VALLEYTRONICS

Imaging of pure spin-valley diffusion current in WS₂-WSe₂ heterostructures

Chenhao Jin,[1]* Jonghwan Kim,[1,2]* M. Iqbal Bakti Utama,[1,3] Emma C. Regan,[1,4]
Hans Kleemann,[1] Hui Cai,[5] Yuxia Shen,[5] Matthew James Shinner,[1]
Arjun Sengupta,[1] Kenji Watanabe,[6] Takashi Taniguchi,[6] Sefaattin Tongay,[5]
Alex Zettl,[1,7,8] Feng Wang[1,7,8]†

Transition metal dichalcogenide (TMDC) materials are promising for spintronic and valleytronic applications because valley-polarized excitations can be generated and manipulated with circularly polarized photons and the valley and spin degrees of freedom are locked by strong spin-orbital interactions. In this study we demonstrate efficient generation of a pure and locked spin-valley diffusion current in tungsten disulfide (WS₂)–tungsten diselenide (WSe₂) heterostructures without any driving electric field. We imaged the propagation of valley current in real time and space by pump-probe spectroscopy. The valley current in the heterostructures can live for more than 20 microseconds and propagate over 20 micrometers; both the lifetime and the diffusion length can be controlled through electrostatic gating. The high-efficiency and electric-field–free generation of a locked spin-valley current in TMDC heterostructures holds promise for applications in spin and valley devices.

Transition metal dichalcogenides (TMDCs) offer a promising platform for applications in spintronics and valleytronics because of their distinctive electronic structure and strong spin-orbital interactions (1–13). At the K and K′ points of the Brillouin zone in TMDCs, two degenerate but inequivalent valleys are present, and these valleys can be used to encode binary information. In addition, spin-orbital coupling leads to locked spin and valley degrees of freedom in TMDC monolayers. The locked spin-valley polarization of charge carriers can exhibit a very long lifetime because intervalley scattering requires a large momentum change and a flip of the spin simultaneously and is therefore a rare event (14–18).

An outstanding challenge in spintronics and valleytronics is to efficiently generate, transport, and detect pure spin-valley current, which will be crucial not only for understanding novel spin-valley physics but also for potential applications in charge-current–free devices with low power consumption (19, 20). In traditional spintronic systems, a transverse spin current is generated through the spin Hall effect in materials with a large spin Hall angle, such as tantalum and tungsten (21–23). Similarly, a transverse valley current has also been realized through the valley Hall effect in TMDC materials, but with low efficiency caused by a small valley Hall angle (13). In both cases a strong driving electric field is necessary, resulting in a dominant and unavoidable longitudinal electric current.

In this study we exploited TMDC heterostructures for efficient optical generation of a pure valley diffusion current without an external electric field, which is accompanied by a pure spin diffusion current because of the spin-valley locking in TMDCs.

Figure 1, A and B, shows an optical microscopy image and a side-view illustration of a representative heterostructure device, respectively. A WSe₂-WS₂ heterostructure (black dashed box in Fig. 1A) is encapsulated in two hexagonal boron nitride (hBN) flakes, with the ~40-nm-thick bottom hBN also serving as the gate dielectric. A few-layer graphene (FLG) back gate is used to tune the carrier concentration in the WSe₂-WS₂ heterostructure, and two FLG source and drain contacts (yellow dashed boxes in Fig. 1A) are symmetrically placed on two sides of the heterostructure. All of the two-dimensional materials were first mechanically exfoliated from bulk crystals and then stacked together by a dry transfer method with a polyethylene terephthalate stamp (24). The whole stack was then transferred onto a 90-nm SiO₂-Si substrate.

We first characterized the gate-dependent optical transitions in the heterostructure by reflection spectroscopy. The results are summarized in Fig. 1C for carrier concentrations ranging from −5 × 10¹²/cm² (hole doping) to 5 × 10¹²/cm² (electron doping). Two prominent resonance features appear around 1.72 and 2.05 eV, corre-

sponding to the A exciton energies in the WSe₂ and WS₂ monolayers, respectively. However, the WSe₂ and WS₂ resonances exhibit distinctively different gate dependencies. Resonances from WSe₂ vary substantially on the hole-doping side, showing both a decrease in the exciton response and an emergence of the trion response, consistent with the behavior of hole-doped monolayer WSe₂ (25, 26). Meanwhile, the WS₂ resonance shows only a slight red shift. The behavior on the electron-doping side is the opposite: only a slight red shift occurs in the WSe₂ resonance, but the WS₂ exciton and trion transitions vary markedly. This peculiar gate dependence can be understood from the type II band alignment (27–29) between WSe₂ and WS₂ (Fig. 1D): The conduction and valence bands in WS₂ are lower than the corresponding bands in WSe₂. Consequently, electrostatically induced electrons and holes will stay only in the WS₂ and WSe₂ layers, respectively.

We then generated a spin-valley current in the hole-doped heterostructures by local circularly polarized laser excitation (Fig. 2, A to D). This mechanism exploits the selective coupling of valley excitons to photon helicity, the ultrafast interlayer charge transfer process, and the ultralong valley hole lifetime in WS₂-WSe₂ heterostructures. First, left-handed circularly polarized photons at 1.80 eV selectively excite K valley excitons in WSe₂. The excited electrons transfer to the conduction band of WS₂ within the first ~100 fs (28, 29), turning off the exciton valley depolarization channel (Maialle-Silva-Sham mechanism) (30) and creating excess valley-polarized holes in the WSe₂ K valley (Fig. 2A) (18). Afterward, electrons in WS₂ recombine with holes in WSe₂ within ~100 ns. As discussed below, the recombinations with K valley and K′ valley holes in WSe₂ have almost equal probabilities (Fig. 2B), which leads to an excess of K valley holes and a deficiency of K′ valley holes in WSe₂ with an ultralong lifetime of many microseconds (Fig. 2C). The local imbalance of valley-polarized holes excited by a focused laser light can drive a pure spin-valley diffusion current (with zero net charge current) through diffusion in the heterostructure (Fig. 2D).

We performed spatial-temporal imaging of the spin-valley current in the WS₂-WSe₂ heterostructure by tracking the valley-polarized holes in the device with space- and time-resolved circular dichroism spectroscopy. An elliptically shaped pump beam at 1.80 eV efficiently generates spin- and valley-polarized holes in the heterostructure, and a second elliptically shaped probe beam at 1.70 eV probes their evolution in space and time by varying both the spatial separation and the temporal delay between the pump and probe pulses (24). Figure 2E displays the profile of the elliptically shaped pump and probe beams at the sample, each with a half width of ~1.5 μm. The temporal delay Δt between the pump and probe pulses is electronically generated by a data acquisition card with 12.5-ns resolution, whereas the spatial separation Δx between the pump and probe pulses

along the width direction is controlled with ~0.2-μm resolution by tuning the angle of a mirror (*24*). The circular dichroic reflection contrast of the probe pulse directly measures the valley-polarized hole density in the heterostructure at

a specific probe position and time (*18*). All experiments were carried out at 10 K.

Figure 2F shows the measured evolution of the valley-polarized hole density in real space and real time for the hole-doped WS₂-WSe₂ heterostructure

at an initial electrostatic hole doping $p_0 = 1 \times 10^{12}/cm^2$. The horizontal and vertical axes represent the temporal and spatial separation between the pump and probe pulses, respectively; the colors represent the amplitude of the circular
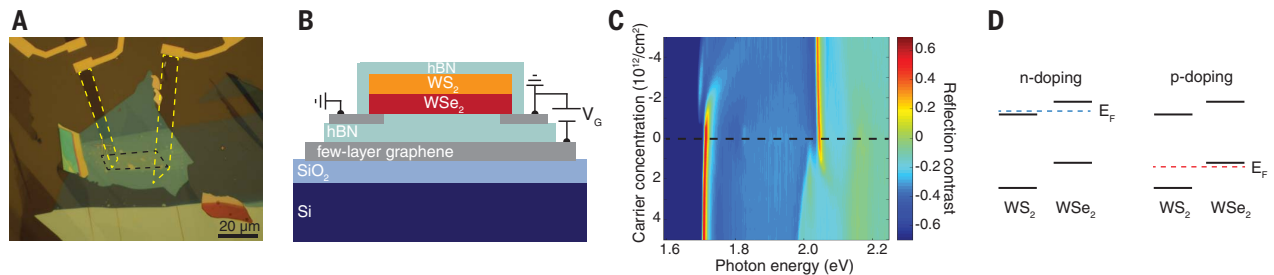

Fig. 1. Gate-dependent optical transitions in the WSe₂-WS₂ heterostructure. (**A** and **B**) Optical microscope image (A) and side-view illustration (B) of the heterostructure device. Black and yellow dashed boxes in (A) mark the heterostructure region and FLG source and drain electrodes, respectively. V_G, gate voltage. (**C**) Doping-dependent reflection contrast of the WSe₂-WS₂ heterostructure. The dashed line indicates charge neutrality. The two prominent resonances around 1.72 and 2.05 eV correspond to the A exciton energies in the WSe₂

and WS₂ monolayers, respectively, which exhibit distinctively different doping dependencies because of the type II band alignment of the heterostructure. (**D**) Type II band alignment of the WSe₂ and WS₂ interface. The conduction band minimum and the valence band maximum reside in WS₂ and WSe₂, respectively. Electrostatically doped electrons stay only in WS₂ for the n-doping case (left panel), whereas holes stay only in WSe₂ for the p-doping case (right panel). E_F, Fermi energy.
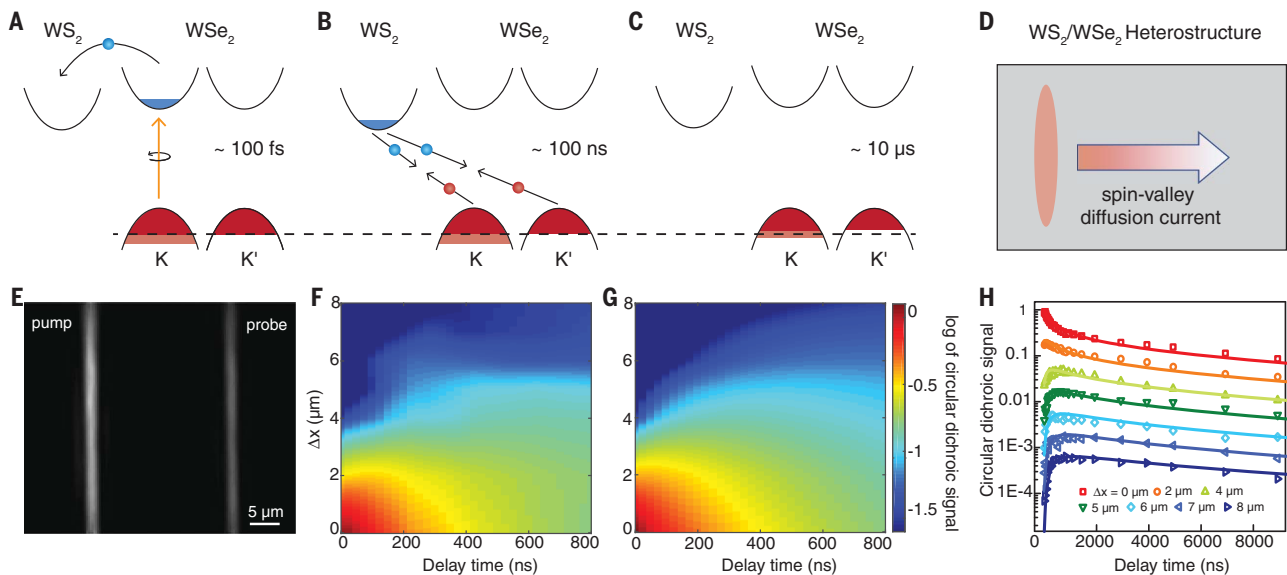

Fig. 2. Pure spin-valley diffusion current in hole-doped WSe₂-WS₂ heterostructures. (**A** to **D**) Experimental scheme for valley current generation in hole-doped WSe₂-WS₂ heterostructures. The dashed line represents the Fermi level before optical excitation. (A) Excitons in the K valley of WSe₂ are selectively excited by circularly polarized pump light and efficiently converted into excess holes within ~100 fs through the ultrafast interlayer charge transfer process. (B) Electrons in WS₂ recombine with K valley and K' valley holes in WSe₂ with almost equal probabilities, resulting in an excess of K valley holes and a deficiency of K' valley holes in WSe₂. (C) This valley-polarized hole population persists for tens of microseconds. (D) Local excitation of such valley-polarized holes can drive a pure valley diffusion current (with zero net charge current) through diffusion in the heterostructure. This pure valley diffusion current will be unidirectional if holes are excited at one edge of the device. (**E** to **H**) Spatial-temporal imaging of the pure spin-valley current. (E) Elliptically shaped pump and probe beam

profiles, each with a ~1.5-μm half width. The long axis of the elliptical light (>50 μm) is much longer than the sample width (~10 μm). Therefore, the illumination is nearly homogeneous along the long axis direction. (F) The spatial-temporal evolution of spin- and valley-polarized holes in the heterostructure with an initial hole doping $p_0 = 1 \times 10^{12}/cm^2$. The horizontal and vertical axes represent the temporal and spatial separation between the pump and probe pulses, respectively. The colors represent the amplitude of the circular dichroism signal on a logarithmic scale, which is proportional to the valley-polarized hole density. The fast decrease in signal at small Δx values and the increase in signal at large Δx values signify the propagation of a valley diffusion current, which can be well captured by simulation from a diffusion-decay model (G). (H) Horizontal cuts from (F) (symbols) and fits from the diffusion-decay model (curves) over a longer time scale. The whole region within Δx = 8 μm becomes homogeneous after 2 μs because of the diffusive valley current and shows an overall slow decay afterward.

dichroism signal on a logarithmic scale. The signal at the origin (corresponding to spatially and temporally overlapped pump and probe pulses) is normalized to 1. At zero time delay, the valley-polarized hole population is localized at the origin with a distribution matching the pump profile (half width of ~1.5 μm), and the circular dichroism signal is negligible at pump-probe separations larger than 3 μm. After a finite delay time, valley-polarized holes start to diffuse out of the excitation region, generating a pure spin-valley diffusion current. This leads to a strong decrease in signal close to the origin but an increase in signal in the region with large pump-probe spatial separation. In particular, a finite signal emerges at $\Delta x > 3$ μm, where no valley polarization is present from the direct pump excitation. As illustrated in Fig. 2F, the valley current can readily propagate to a distance of more than 8 μm within a time period of 800 ns.

We can compare the measured spatial-temporal image of the valley-polarized hole density to diffusion theory and extract important dynamic transport parameters. The spatial-temporal evolution of the one-dimensional valley-polarized hole density $\Delta p_v(x, t)$ is described by a simple diffusion-decay model (24)

$$\Delta p_v(x,t) = \frac{\Delta p_0}{\sqrt{\pi(\sigma_0^2 + 4Dt)}} e^{-\frac{x^2}{\sigma_0^2 + 4Dt}} e^{-\frac{t}{\tau}} \qquad (1)$$

where Δp_0 is the total number of pump-induced spin- and valley-polarized holes, σ_0 is the half width of the pump beam, D is the hole diffusion constant, and τ is the lifetime of valley-polarized holes (limited by a finite intervalley scattering time). The pump-probe signal $S(\Delta x, \Delta t)$ can be calculated by convolving $\Delta p_v(x, \Delta t)$ with the probe beam intensity $T(x)$ at a given pump-probe separation Δx (24). Figure 2G shows the simulated pump-probe signal with a hole diffusion constant of $D = 0.2$ cm^2/s and a valley lifetime of $\tau = 20$ μs. The excellent agreement between the experimental and theoretical results confirms the diffusion-dominated dynamics of valley-polarized holes. Figure 2H shows several horizontal line cuts of Fig. 2F over a longer time scale (different curves are shifted vertically and successively by 40% of the major tick separation for visual clarity; fig. S2 illustrates vertical line cuts). We observed that the whole region within $\Delta x = 8$ μm became homogeneous after 2 μs because of the diffusive valley current and exhibited an overall slow decay afterward. This dynamic is well captured by the diffusion-decay model in Eq. 1 (curves in Fig. 2H). The valley lifetime of $\tau = 20$ μs extracted here is more than one order of magnitude longer than the earlier reported values (14–18). From the valley hole diffusion constant and valley polarization lifetime, we obtain a valley diffusion length of $l = \sqrt{D\tau} = 20$ μm. In addition, the optical generation can produce a very high valley current density, reaching 2×10^7 A/m^2 in the ~1-nm-thick heterostructure at a valley-polarized hole density of 10^{12}/cm^2 (24).

The photo-generated valley diffusion current can be modulated substantially through electrostatic gating. Figure 3, A and C, shows the spatial-temporal mapping of the valley-polarized hole density with the initial hole doping at ~0 and 2.8×10^{12}/cm^2, respectively. We found that the valley-polarized hole density decays over time but maintains the same spatial profile for near-zero initial doping (Fig. 3A). This indicates that at the low-doping limit valley-polarized holes are largely localized and there is no valley current. In contrast, the valley diffusion current flow becomes quite large for the highly hole-doped heterostructure at 2.8×10^{12}/cm^2 (Fig. 3C), leading to a peak spin-valley diffusion current density of 1.2×10^8 A/m^2 at a valley-polarized hole density of 10^{12}/cm^2 (24).

Figure 3, B and D, shows theoretical modeling of the valley hole diffusion at $p_0 = 0$ and 2.8×10^{12}/cm^2, respectively. The extracted diffusion constants are summarized in Fig. 3E. From the diffusion constant, we can directly obtain the density-dependent hole mobility using the Einstein relation for a Fermi liquid at 10 K (24). The holes are almost completely localized at a doping level close to the charge neutrality point. Therefore, both the diffusion constant and the mobility are negligibly small. At larger carrier concentrations, the hole diffusion constant and the mobility both increase substantially, reaching $D = 1.2$ cm^2/s and $\mu = 160$ cm^2/(V · s) at $p_0 = 2.8 \times 10^{12}$/cm^2. The localization of holes at low carrier density signifies a mobility edge in TMDC materials, which may be related to Anderson localization from potential fluctuations (31). Traditional low-temperature transport measurements at such low carrier concentrations are quite challenging or almost impossible because of an exponentially large contact resistance. In this study the spatially and temporally resolved optical imaging provided a contact-free approach to measure the intrinsic charge transport in TMDCs, and it can be a powerful and general tool for characterizing the transport behavior of two-dimensional systems at low carrier concentrations.

Like the hole diffusion constant, the valley-polarized hole lifetime also depends strongly on the electrostatic gating. Notably, the valley-polarized hole population ($\Delta p_v \equiv \Delta p_K - \Delta p_{K'}$), where Δp_K and $\Delta p_{K'}$ are photo-generated excess hole densities in the K and K' valleys of WSe$_2$, respectively, can exhibit very different behavior from the total excess hole population ($\Delta p_{tot} \equiv \Delta p_K + \Delta p_{K'}$). The different dynamic behaviors of Δp_{tot} and Δp_v can be probed from the sum and difference responses of left and right circularly polarized probe light, respectively (18). Figure 4A shows the population decay of the total excess holes in the heterostructure at $\Delta x = 0$ for different initial carrier concentrations, with the decay constants summarized in Fig. 4B (triangles). The decay lifetime of Δp_{tot} ranges from 20 to 500 ns and becomes shorter at both greater electron doping and greater hole doping of the heterostructures. In contrast, the valley-polarized hole lifetime (circles in Fig. 4B) is the same as the total hole population lifetime for charge-neutral and electron-doped heterostructures but decouples and becomes much longer for hole-doped cases.

The unusual dynamics of doping-dependent valley lifetime arises from the distinctive interlayer electron-hole recombination process in the heterostructure, as illustrated in Fig. 4, C and D (24). For electron-doped or charge-neutral heterostructures (Fig. 4C), all of the holes in WSe$_2$ are pump-generated "excess holes." Therefore, when Δp_{tot} decays to zero because of interlayer electron-hole recombination, no holes—and certainly no valley-polarized holes—remain in the WSe$_2$. In these cases, the valley lifetime is limited by the total excess hole lifetime. The scenario is completely different for hole-doped heterostructures (Fig. 4D). If the original hole density is much larger than the photo-generated one,
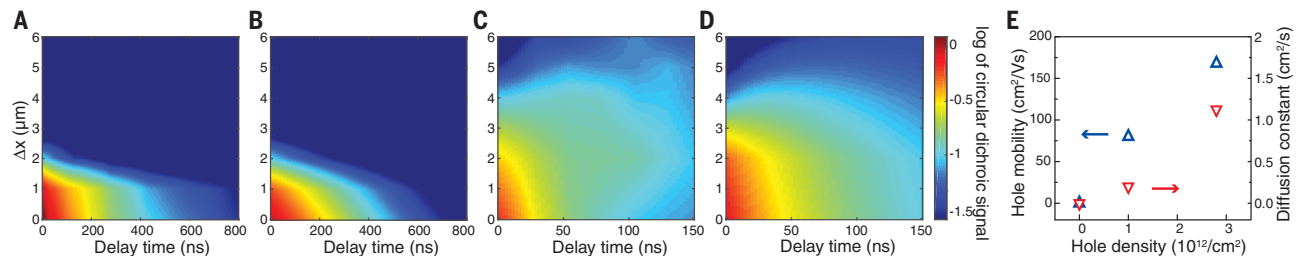

Fig. 3. Strong modulation of spin-valley current with electrostatic gating. (**A** and **C**) Spatial-temporal imaging of spin-valley current at initial hole concentrations of near zero (A) and 2.8×10^{12}/cm^2 (C). (**B** and **D**) Corresponding simulation results from the diffusion-decay model. The valley-polarized holes have negligible diffusion near the charge-neutral point (A and B). In contrast, holes diffuse efficiently at large hole doping (C and D), creating a large spin-valley current density up to 1.2×10^8 A/m^2 at an optical excitation density of 10^{12}/cm^2. (**E**) Extracted hole diffusion constant (red) and mobility (blue) show a strong dependence on the initial hole concentration.
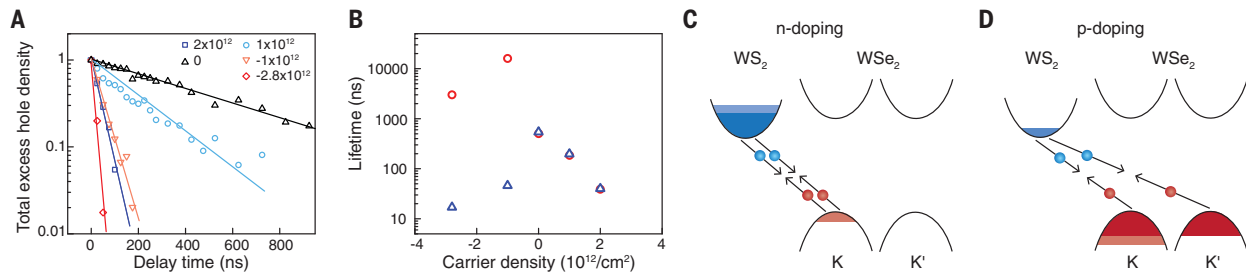
Fig. 4. Doping-dependent lifetime of total excess hole and valley-polarized hole populations. (**A**) Decay dynamics of the total excess hole density at different initial carrier concentrations. The decay lifetime is longest near charge neutrality and decreases with both electron doping (positive carrier concentration) and hole doping (negative carrier concentration). (**B**) Comparison between valley-polarized hole lifetime (circles) and total excess hole lifetime (triangles). The valley lifetime is limited by the total population lifetime in charge-neutral and electron-doped heterostructures; in hole-doped heterostructures the valley lifetime can be orders of magnitude longer than the total excess hole lifetime. (**C**) For electron-doped or charge-neutral heterostructures, interlayer electron-hole recombination directly reduces the valley-polarized hole density. Dark and light blue colors represent the electrostatically injected electrons and photo-generated electrons, respectively. (**D**) If the initial hole doping density (dark red) is much larger than the photo-generated one (light red), electrons in WS_2 (blue) will recombine with holes at K and K' valleys of WSe_2 with almost equal probabilities, reducing only the total excess hole population but not the valley-polarized hole density.

excess electrons in WS_2 will recombine with holes from both valleys of WSe_2 with almost equal probabilities (24). Consequently, the valley-polarized hole density Δp_v decouples from the net excess hole population Δp_{tot} and persists long after the latter decays to zero, enabling the generation of a pure spin-valley diffusion current.

The generation efficiency of a pure spin-valley diffusion current in our heterostructure-based device can be very high because of the near-perfect conversion from optical excitation to the pure valley diffusion current (24). Because of the lack of any associated charge current in our device, the pure spin-valley diffusion current density scales linearly with the optical excitation power, as opposed to the square-root scaling with power for electrically generated current. Therefore, the power efficiency of heterostructure devices can be favorable for generating large spin and valley current. Along with the ultralong spin-valley lifetimes and diffusion lengths, TMDC heterostructures provide exciting opportunities to realize future spintronic and valleytronic devices.

REFERENCES AND NOTES

1. D. Xiao, G. B. Liu, W. Feng, X. Xu, W. Yao, *Phys. Rev. Lett.* **108**, 196802 (2012).
2. X. Xu, W. Yao, D. Xiao, T. F. Heinz, *Nat. Phys.* **10**, 343–350 (2014).
3. T. Cao *et al.*, *Nat. Commun.* **3**, 887 (2012).
4. H. Zeng, J. Dai, W. Yao, D. Xiao, X. Cui, *Nat. Nanotechnol.* **7**, 490–493 (2012).
5. K. F. Mak, K. He, J. Shan, T. F. Heinz, *Nat. Nanotechnol.* **7**, 494–498 (2012).
6. Y. Li *et al.*, *Phys. Rev. Lett.* **113**, 266804 (2014).
7. E. J. Sie *et al.*, *Nat. Mater.* **14**, 290–294 (2015).
8. D. MacNeill *et al.*, *Phys. Rev. Lett.* **114**, 037401 (2015).
9. J. Kim *et al.*, *Science* **346**, 1205–1208 (2014).
10. A. Srivastava *et al.*, *Nat. Phys.* **11**, 141–147 (2015).
11. Z. L. Ye, D. Z. Sun, T. F. Heinz, *Nat. Phys.* **13**, 26–29 (2017).
12. G. Aivazian *et al.*, *Nat. Phys.* **11**, 148–152 (2015).
13. K. F. Mak, K. L. McGill, J. Park, P. L. McEuen, *Science* **344**, 1489–1492 (2014).
14. L. Yang *et al.*, *Nat. Phys.* **11**, 830–834 (2015).
15. W.-T. Hsu *et al.*, *Nat. Commun.* **6**, 8963 (2015).
16. X. Song, S. Xie, K. Kang, J. Park, V. Sih, *Nano Lett.* **16**, 5010–5014 (2016).
17. P. Rivera *et al.*, *Science* **351**, 688–691 (2016).
18. J. Kim *et al.*, *Sci. Adv.* **3**, e1700518 (2017).
19. S. Murakami, N. Nagaosa, S. C. Zhang, *Science* **301**, 1348–1351 (2003).
20. I. Žutić, J. Fabian, S. Das Sarma, *Rev. Mod. Phys.* **76**, 323–410 (2004).
21. J. Sinova, S. O. Valenzuela, J. Wunderlich, C. H. Back, T. Jungwirth, *Rev. Mod. Phys.* **87**, 1213–1260 (2015).
22. L. Liu *et al.*, *Science* **336**, 555–558 (2012).
23. C. F. Pai *et al.*, *Appl. Phys. Lett.* **101**, 122404 (2012).
24. See supplementary materials.
25. K. F. Mak *et al.*, *Nat. Mater.* **12**, 207–211 (2013).
26. Z. Wang, J. Shan, K. F. Mak, *Nat. Nanotechnol.* **12**, 144–149 (2017).
27. J. Kang, S. Tongay, J. Zhou, J. B. Li, J. Q. Wu, *Appl. Phys. Lett.* **102**, 012111 (2013).
28. X. Hong *et al.*, *Nat. Nanotechnol.* **9**, 682–686 (2014).
29. F. Ceballos, M. Z. Bellus, H.-Y. Chiu, H. Zhao, *ACS Nano* **8**, 12717–12724 (2014).
30. M. Z. Maialle, E. A. de Andrada e Silva, L. J. Sham, *Phys. Rev. B* **47**, 15776–15788 (1993).
31. P. W. Anderson, *Phys. Rev.* **109**, 1492–1505 (1958).

Science

Imaging of pure spin-valley diffusion current in WS$_2$-WSe$_2$ heterostructures

Chenhao Jin, Jonghwan Kim, M. Iqbal Bakti Utama, Emma C. Regan, Hans Kleemann, Hui Cai, Yuxia Shen, Matthew James Shinner, Arjun Sengupta, Kenji Watanabe, Takashi Taniguchi, Sefaattin Tongay, Alex Zettl and Feng Wang

Tracking the spin-valley current
Taking advantage of the electron's spin and valley degrees of freedom requires a method for generating currents of carriers that have a particular spin or come from a particular valley in the electronic structure. Jin *et al.* used a heterostructure made out of adjacent layers of WSe$_2$ and WS$_2$ to create a spin-valley diffusion current without applying an external electric field. Instead, they used circularly polarized laser light to initiate the diffusion and a second laser pulse to image the propagation of the carriers. With long lifetimes and diffusion lengths, the method may be of practical use in future valleytronic devices.
Science, this issue p. 893

ARTICLE TOOLS	http://science.sciencemag.org/content/360/6391/893
SUPPLEMENTARY MATERIALS	http://science.sciencemag.org/content/suppl/2018/05/23/360.6391.893.DC1
REFERENCES	This article cites 32 articles, 7 of which you can access for free http://science.sciencemag.org/content/360/6391/893#BIBL
PERMISSIONS	http://www.sciencemag.org/help/reprints-and-permissions

Use of this article is subject to the Terms of Service